

**Vortex entropy and superconducting fluctuations in ultrathin
underdoped $\text{Bi}_2\text{Sr}_2\text{CaCu}_2\text{O}_{8+x}$ superconductor**

Shuxu Hu¹, Jiabin Qiao^{1,2,3*}, Genda Gu⁴, Qi-Kun Xue^{1,3,5,6*}, and Ding Zhang^{1,3,6,7*}

¹State Key Laboratory of Low Dimensional Quantum Physics and Department of Physics, Tsinghua University, Beijing 100084, China

²Centre for Quantum Physics, Key Laboratory of Advanced Optoelectronic Quantum Architecture and Measurement, School of Physics, Beijing Institute of Technology, Beijing 100081, China

³Beijing Academy of Quantum Information Sciences, Beijing 100193, China

⁴Condensed Matter Physics and Materials Science Department, Brookhaven National Laboratory, Upton, NY 11973, USA

⁵Southern University of Science and Technology, Shenzhen 518055, China

⁶Frontier Science Center for Quantum Information, Beijing 100084, China

⁷RIKEN Center for Emergent Matter Science (CEMS), Wako, Saitama 351-0198, Japan

* E-mail: jiabinqiao@bit.edu.cn; qkxue@mail.tsinghua.edu.cn;
dingzhang@mail.tsinghua.edu.cn

Abstract

Vortices in superconductors can help identify emergent phenomena but certain fundamental aspects of vortices, such as their entropy, remain poorly understood. Here, we study the vortex entropy in underdoped $\text{Bi}_2\text{Sr}_2\text{CaCu}_2\text{O}_{8+x}$ by measuring both magneto-resistivity and Nernst effect on ultrathin flakes (≤ 2 unit-cell). We extract the London penetration depth from the magneto-transport measurements on samples with different doping levels. It reveals that the superfluid phase stiffness ρ_s scales linearly with the superconducting transition temperature T_c , down to the extremely underdoped case. On the same batch of ultrathin flakes, we measure the Nernst effect via on-chip thermometry. Together, we obtain the vortex entropy and find that it decays exponentially with T_c or ρ_s . We further analyze the Nernst signal above T_c in the framework of Gaussian superconducting fluctuations. The combination of electrical and thermoelectric measurements in the two-dimensional limit provides fresh insight into high temperature superconductivity.

Superconducting vortices, each made of a swirling supercurrent around a normal core, are vital entities not only for understanding crucial aspects of their host superconductors¹⁻⁴ but also for realizing novel functions⁵⁻⁹. Vortices played a central role in generating the diode effect in asymmetric superconductors¹⁰⁻¹¹. This so-called vortex ratchet effect has been further developed for constructing a supercurrent diode¹², which can switch between dissipationless and dissipative states by the bias direction. Of late, investigating vortices are indispensable for identifying the topological nature of a superconductor via Majorana zero modes¹³⁻¹⁷. These advancements call for a deeper understanding of vortices. One powerful approach to meeting this goal is by applying a temperature gradient ($-\nabla_x T$) along the superconductor¹⁸⁻²⁰ to drive a vortex flow below the superconducting transition temperature (T_c). The temperature gradient exerts a thermal force on the vortex: $F = -S_d \nabla_x T$, where S_d is the transport entropy per vortex. Due to the motion of vortices, a transverse electric field, i.e., $E_y = B v_x$ (v_x is the velocity of vortices along the temperature gradient), is produced and can be experimentally measured. As a result, the Nernst effect, defined as $N = E_y / (-\nabla_x T)$, can probe directly the vortex dynamics. Such a scheme has been employed to extract S_d by using the formula^{18,19,21}: $S_d = N \Phi_0 / \rho_{xx}$, where $\Phi_0 = h/2e$ is the flux quantum and ρ_{xx} is the flux-flow resistivity.

A recent study collected the data of S_d from four distinct families of superconductors, ranging from Nb-SrTiO₃ with a rather low T_c of 0.35 K to La_{2-x}Sr_xCuO₄ with a T_c as high as 29 K²². Interestingly, the sheet entropy, defined as $S_d^{sheet} = S_d c$ (c is the c -axis lattice constant) seems to be comparable among the four superconductors at the peak position of the Nernst signal. This investigation was soon extended to two other cuprate compounds: YBa₂Cu₃O_{6+x} and Bi₂Sr₂CaCu₂O_{8+x} (BSCCO), with T_c around 90 K²³, and the isotropic superconductor of K₃C₆₀²⁴. So far, these studies employed compounds in individual superconducting families with the optimal T_c . However, many of these unconventional superconductors have a dome-like dependence of T_c as a function of doping. The doping evolution of vortex entropy

is thus an outstanding problem that calls for experimental investigations.

Measuring the Nernst effect has also shed vital insights into the superconducting fluctuations in numerous superconductors²⁵⁻²⁹ above the transition temperature ($T > T_c$). Xu *et al.*²⁵ first attributed the strongly enhanced Nernst signal above T_c to superconducting fluctuations in the pseudogap regime. Of late, Cyr-Choinière *et al.*²⁶ pointed out that superconducting fluctuations only extend above T_c to a narrow temperature window, which is far below the pseudogap temperature. Still, data points demarcating the onset of superconducting fluctuations remain limited in the phase diagram and the extremely underdoped regime (EUD) has not been explored.

Here, we address the doping dependence of vortex entropy in BSCCO with their thicknesses down to 1.5 unit-cell (UC). Pushing to the 2D limit allows us to address electrical and thermoelectric transport in highly uniform samples even in the EUD regime ($T_c \sim 7$ K). A comparative study of ultrathin and bulk-like samples clearly reveals the dimensionality effect in thermal activation of vortices. Studying the samples in the 2D limit allows us to extract quantitatively the London penetration depths. By combining the magneto-resistance and Nernst effect data from the same batch of samples, we obtain the vortex sheet entropy S_d^{sheet} from the optimally doped (OP) to the EUD regime. Notably, S_d^{sheet} dramatically plummets with decreasing doping, showing an exponential dependence on T_c . Furthermore, the prominent Nernst signal above T_c extends to a limited range of about 40 K in the EUD case. Our data can be further compared with the theory for Gaussian superconducting fluctuations. In general, our work opens up further opportunities in addressing vortex dynamics and superconducting fluctuations in 2D superconductors.

Results

Sample fabrication. Cuprate superconductors in the underdoped regime often suffer from inhomogeneity and even phase separation. In order to study samples with high

uniformity, we take advantage of the recent development in fabricating ultrathin BSCCO samples³⁰⁻³⁴. We tune the doping levels by the controlled release of oxygen, as displayed in Fig. 1a. This recipe starts with a prepatterned SiO₂/Si substrate (Fig. 1b). Its electrodes, for both standard transport and on-chip thermometry, are already wired to a chip carrier (Fig. 1a). In the inert atmosphere, we dry stamp the selected BSCCO flake onto the electrodes (further details are given in Methods). For ultrathin BSCCO flakes (1.5-2 UC thick), in contrast to thick ones, their doping level can move to the EUD regime once landed on the substrate. This is caused by out-diffusion of interstitial oxygen at room temperature³². After a controlled period of time (up to 30 mins), we cap BSCCO with a flake of hexagonal boron nitride (h-BN) to suppress this out-diffusion and protect the sample against further degradation. The complete setup is quickly loaded into the cryostat (within 5 mins) for measurements. The oxygen out-diffusion is eventually switched off by cooling the sample to low temperatures. We employ our recipe to realize a set of ultrathin BSCCO samples with their doping levels ranging from OP to EUD. Their temperature dependent resistance curves are displayed in Fig. 1c. We define their T_c from the temperature point where the resistance first reaches 1% of the normal state resistance with decreasing temperature (see details in Supplementary Note 5). This criterion is consistent with former studies on bulk superconductors²⁸. Notably, superconducting transitions measured from different pairs of contacts on the same sample show nearly indistinguishable behaviors, attesting to the high uniformity.

Magneto-resistivity and superfluid phase stiffness. Figure 2a-e presents the magneto-resistivity from the ultrathin samples and Figs. 2f, g shows similar data but from bulk-like flakes. For each sample, we measure the temperature dependent resistivity at a set of perpendicular magnetic fields (along the *c*-axis). We first compare ultrathin and bulk-like samples in the OP regime (Fig. 2a and Fig. 2f). Instead of a monotonic temperature dependence as seen in sample S1, a shoulder develops in the transition regime (60-80 K) of S6 with the applied magnetic fields. Such a shoulder was

observed in early measurements of bulk BSCCO^{35,36} and was later understood as an indication of current redistribution³⁷. Applying a magnetic field enhances the anisotropic factor ρ_c/ρ_{ab} , where ρ_c and ρ_{ab} are out-of-plane and in-plane resistivity components. Consequently, the current gets squeezed to the layers closer to the bottom contacts (Inset of Fig. 2f). The absence of any shoulder in the data of S1 to S5 demonstrates the superiority of using ultrathin samples. By getting rid of the current redistribution problem, the measured resistivity reliably reflects the in-plane component. Comparison in the underdoped (UD) regime shows another advantage of ultrathin samples. Figure 2g shows the typical behavior of UD samples fabricated from an as-grown UD crystal. Resistivity increases with decreasing T in the normal state before the superconducting transition. By contrast, the ultrathin samples at the same doping and even lower doping exhibit fully metallic behavior in the normal state (Fig. 2d,e), attesting to substantially improved homogeneity.

From the magnetic field response, we can define a temperature point where the resistivity traces bifurcate (indicated by arrows in Fig. 2a-e). This temperature point reflects the onset of superconductivity. The difference between this onset and T_c reflects the broad superconducting transition. Such a difference increases with decreasing doping. For samples S3 and S4, the onset temperature is roughly 20 K above T_c whereas for sample S5 this temperature window is about 30 K. It indicates enhanced superconducting fluctuations in the EUD regime.

The resistivity data helps probe deeper into the vortex dynamics and the dimensionality effect. In the superconducting transition region, ρ_{xx} stems from the thermally activated flux flow (TAFF) such that: $\rho_{xx} \propto \exp(-U/k_B T)$, where U is the activation energy of vortices. Notably, our ultrathin samples show linear dependences between U and B in the semilogarithmic plot (Fig. 2h), demonstrating that $U \propto \ln B$. This is strikingly different from the typical power law dependence $U \propto B^{-\alpha}$ of bulk samples (Supplementary Figure 4). This qualitative difference reflects a drastic

change in the vortex dynamics. Vortices in a multilayer system tend to align along the c -axis and form flux lines. Thermal activation deforms these flux lines³⁸. For the ultrathin BSCCO, however, thermal activation is governed by the collective creeping of vortices³⁹ in a 2D plane. Our work therefore reveals clearly the dimensionality crossover in high temperature cuprate superconductors from multi-layer to the atomic limit.

Based on the 2D vortex creeping model, the slope of each line in Fig. 2h is directly proportional to the superfluid phase stiffness ρ_s (see details in Methods), which is further related to the London penetration depth λ because $\rho_s \propto 1/\lambda^2$. A decreasing slope in Fig. 2h with lower T_c therefore directly reflects reduced ρ_s with decreased doping. This is summarized in Fig. 2i. Within a wide range of doping, we observe that ρ_s behaves rather linearly with T_c , consistent with the relation⁴⁰ first proposed by Uemura *et al.* Our results thus extend the linear relation to the 2D limit and in the EUD situation. Apart from the linear behavior, we extract quantitatively the London penetration depth λ (Fig. 2j). The values near OP are consistent with those determined by using bulk-sensitive techniques⁴¹⁻⁴³. Moreover, the magneto-transport measurements yield quantitative information of λ in the previously inaccessible EUD regime.

Nernst effect and vortex entropy. After characterizing the magneto-resistivity, we study Nernst effect on the same batch of samples. We sweep the magnetic field at fixed temperatures and registering the transverse voltage induced by a temperature gradient. Figure 3a1-a5 shows the representative traces of the Nernst signal N . We note that the results for S1 are in quantitative agreement with previous experiments¹⁸ on bulk crystals at OP. The measured Nernst values in ultrathin samples are also consistent with those obtained from thicker flakes by using the same on-chip setup (Supplementary Figure 5b1). This is different from the dichotomy in magneto-resistivity data, because thermoelectric measurements on relatively thick samples do

not suffer from the current redistribution problem. In addition, the Seebeck coefficients of S1 to S5 (Supplementary Fig. 6), measured essentially in the normal state at $T \gg T_c$, show behaviors consistent with previous reports (Supplementary Note 3), further confirming the reliability of our on-chip thermometry.

In Fig. 3b1-b5, we plot the temperature dependence of N at selected magnetic fields, showing a typical peak profile. Notably, the peak value of N from samples with drastically different doping levels are on the same order of magnitude (a few $\mu\text{V/K}$). This echoes with the recent observation by Rischau *et al.*²² There, peak values of N were reported to be 4-10 $\mu\text{V/K}$ among six different superconducting compounds. In contrast to the nearly invariant peak height, the peak position ($T_{N,p}$) relative T_c shows a clear evolution from Fig. 3b1 to Fig. 3b5. $T_{N,p}$ stays below T_c (dashed line) in S1 and S2 but becomes nearly coincident with T_c for S3 and S4 with reduced doping. In the EUD sample S5, the peak position $T_{N,p} = 20$ K obviously exceeds $T_c = 7.1$ K but remains below the onset temperature for superconductivity.

We combine the data in Fig. 2a1-a5 and Fig. 3b1-b5 and calculate the off-diagonal Peltier coefficient $\alpha_{xy} = N/\rho_{xx}$ (Fig. 3c1-c5). We verify in Supplementary Fig. 7 that ρ_{xx} and N below T_c are measured in the linear response regime. The temperature dependence of α_{xy} at a fixed B also exhibits a peak, similar to that of N . The peak position of α_{xy} is at a lower temperature than that of the corresponding Nernst peak, i.e., $T_{\alpha,p} < T_{N,p}$. For samples S1 to S4, $T_{\alpha,p}$ is deep below T_c . For S5, only data at 5 K is below T_c (we discuss the contribution from superconducting fluctuations in the discussion section). The prominent signal of N or α_{xy} below T_c reflects vortex motion in the liquid state. Further lowering the temperature may drive the system into the vortex lattice phase such that α_{xy} diminishes. At around $T_{N,p}$ for S1 to S4 and at 5 K for S5, ρ_{xx} vanishes at zero magnetic field and grows linearly with B across a wide field range (Supplementary Fig. 8). This trend agrees with the flux flow (FF) behavior: $\rho_{xx} = B\Phi_0/\eta$ for a constant η . We remark that FF occurs at a relatively

higher temperature and magnetic field than the regime for the TAFF, in which we extract the superfluid stiffness in the previous section. From sample S1 to S5, we observe that α_{xy} in this regime, which is directly linked to the vortex entropy via: $S_d = \Phi_0 \alpha_{xy}$, shows a clear drop in orders of magnitude with decreasing doping (from Fig. 3c1 to Fig. 3c5). It indicates a sharp decrease of vortex entropy with reduced doping. In fact, a constant entropy, i.e., a fixed ratio between N and the measured ρ_{xx} , would require a large N on the order of $100 \mu\text{V/K}$ in the EUD regime, exceeding the typical value recorded in superconductors by at least one order of magnitude^{19,44}.

In Fig. 4a, we compare the sheet entropy $S_d^{sheet} = S_d c$ (c is the c -axis lattice constant) in samples S1 to S5 with those from other superconductors. For S1 to S4, we extract S_d^{sheet} at $T_{N,p}$ and at the highest magnetic field applied. For sample S5, the resistivity data may be contaminated by quasi-particle scattering at $T_{N,p}$ because $T_{N,p} > T_c$. We thus choose the data obtained below T_c (at 5 K). As shown in Fig. 4a, a great variety of superconductors with a wide range of T_c possess S_d^{sheet} values clustering around k_B (dashed line). At OP, our measured S_d^{sheet} is in agreement with the former study on BSCCO films²³. In the EUD regime, however, the vortex entropy of BSCCO becomes two orders of magnitude smaller than that of NbSe₂ with a similar T_c . Theoretically, the vortex entropy can be evaluated from the condensation energy of the normal core⁴⁵ (see details in Methods): $S_d^{cal} \sim \frac{\Phi_0^2}{\lambda^2 T_c}$. Based on the experimentally determined λ and T_c , the theoretically expected value is $21k_B$ at OP. The theoretical value is 10 times the experimental one ($2k_B$). This is different from the previous report²², which shows 50 times difference between theory and experiment for Nb-SrTiO₃.

Importantly, there exists a monotonic decrease of S_d^{sheet} in BSCCO with decreasing T_c . Such a decrease is unexpected in theory (squares in Fig. 4a). $S_d^{cal} \sim \frac{\Phi_0^2}{\lambda^2 T_c}$ should be insensitive to doping because $\lambda^2 T_c$ is a constant ($1/\lambda^2 \propto T_c$ confirmed in Fig. 2i).

Intriguingly, the experimental doping dependence can be nicely captured by an exponential relation: $S_d^{sheet} \propto \exp(T_c/T_0)$, with $T_0 \sim 12$ K. It manifests itself in the semilogarithmic plot of Fig. 4a as a straight line (gray). Furthermore, our thermal activation study indicates that the superfluid density n_s or ρ_s has a linear relation with T_c . Therefore, the exponential relation of entropy vs. T_c may also indicate that $S_d^{sheet} \propto \exp(n_s)$. Such a quantitative relation may guide further theoretical investigations.

Discussion

We observe systematically reduced vortex entropy with decreasing doping. State-of-the-art scanning tunneling microscopy studies on cuprates have revealed intriguing ordering⁴⁶⁻⁴⁸ such as pair density waves inside the vortices. Such a symmetry breaking effect, of either spin or charge, is not taken into account by the simple theoretical model that calculates the superconducting condensation energy. These orderings may lead to reduced entropy. However, the spin density wave emerges only in the EUD regime close to the antiferromagnetic insulator phase. It seems unlikely to play a major role at a doping level $p \sim 0.1$, at which the vortex entropy is already smaller than that at optimal doping. For the charge ordering, it is most prominent around the doping level of $p = 0.125$ and weakens if p departs from 0.125. This non-monotonic doping dependence is incompatible with the observation of a monotonic decrease of the vortex entropy across the underdoped regime. In general, the entropy reduction seems unrelated to the well-studied spin or charge ordering.

We also discuss the implication of our experiments on the boundary of superconducting fluctuations in the phase diagram. We employ a similar protocol of Cyr-Choinière *et al.*²⁶ and determine a temperature point— T_b —above which the signal from superconducting fluctuations drops below our measurement noise level (marked in Fig. 3b1-b5, see details in Supplementary Note 6). Furthermore, we also obtain the temperature T_{cr} where the Nernst signal changes sign. This temperature can also

mark the dominance of the contribution from quasi-particles²⁶. Figure 4b summarizes T_b and T_{cr} over half of the superconducting dome in BSCCO. The temperature window ($T_b - T_c$) for superconducting fluctuations broadens from 5 K at OP to 40 K at EUD. Even for BSCCO in the 2D limit, the temperature regime for prominent superconducting fluctuations lies well within the pseudogap region, consistent with the finding in other cuprate bulk crystals²⁶.

Quantitatively, the theory of Gaussian superconducting fluctuations (GSF) yields^{49,50}:

$$\alpha_{xy}^{GSF}/B \sim \frac{k_B e^2 (\xi_{ab}^0)^2}{6\pi\hbar^2 s} t^{-1},$$

where $B \ll B_{c2}$, $\xi_{ab,c}^0$ is the in-plane coherence length, $t = T/T_c - 1$ is the reduced temperature, and s is the interlayer spacing. Past studies indicate that this simple formula agree quantitatively with the experimental data from superconductors of $\text{Nb}_x\text{Si}_{1-x}$ ²⁷, $\text{La}_{1.8-x}\text{Eu}_{0.2}\text{Sr}_x\text{CuO}_4$ (Eu-LSCO)²⁸, $\text{Pr}_{2-x}\text{Ce}_x\text{CuO}_4$ ²⁹, etc. It is therefore interesting to check its validity in BSCCO—a superconductor with much more pronounced anisotropy. Supplementary Fig. 12 compares the Nernst coefficient data of S3 to S5 with the GSF formula. There exists reasonable agreement in a temperature window above T_c , indicating a dominant contribution of GSF over other factors such as quasi-particles, spin or charge order. Moreover, the fitting parameter ξ_{ab}^0 is consistent with the estimated coherence length based on magneto-transport. Strong deviation occurs at elevated temperatures ($T \sim 1.4T_c$ for S3, S4, and $T \sim 4T_c$ for S5), suggesting the dominance of quasi-particles at relatively high temperatures. This crossover again reflects the limited temperature region for superconducting fluctuations.

In summary, we carry out an extensive transport study of BSCCO in the 2D limit and from OP to EUD. The simultaneously measured magneto-resistivity and Nernst effect allow us to extract key physical parameters such as the superfluid phase stiffness/London penetration depth, the vortex entropy, and the temperature window for apparent superconducting fluctuations. While the superfluid phase stiffness varies linearly with doping, the vortex entropy decreases exponentially at lower T_c . The

Nernst signal covering half of the superconducting dome also helps settle the long-standing controversy over superconducting fluctuations in bismuth-based high- T_c superconductors. Probing electrical and thermoelectric properties in ultrathin BSCCO sets a paradigm for gaining a comprehensive and decisive understanding of emergent properties of 2D superconductivity.

Methods

Sample fabrication. To standardize the on-chip thermometry, we patterned a complete 4-inch silicon wafer with 285 nm thick SiO₂ by using photolithography and electron beam evaporation of metals (Ti/Au: 5 nm/35 nm). The wafer was then diced into rectangular substrates 10 × 4 mm². Each substrate hosts the same design of electrodes for both resistivity measurements and on-chip thermometry⁵¹. The inset in Supplementary Fig. 1a illustrates the configuration of electrodes on one such substrate. A meandering line on the top served as the heater. Two metal strips with a width of 2 μm were placed next to the heater as local thermometers (each of them has four leads). They were also used as source and drain in the resistivity measurements of the sample. Four additional electrodes were placed in between the thermometers for registering the longitudinal and transverse voltages of the sample. Prior to the stamping of BSCCO, each substrate was glued to a chip carrier with its electrodes electrically wired to the pins.

Single crystals of BSCCO were grown by the traveling floating zone method. Exfoliation and dry-transfer of BSCCO were then carried out in a glovebox with Ar atmosphere (H₂O < 0.1 ppm, O₂ < 0.1 ppm)³⁴. We realized ultrathin samples from either the optimally doped (S2-S5) or overdoped (S1) single crystals. Each sample is with a fixed doping level realized by controlled oxygen release and subsequent quenching at low temperatures. In principle, the release of oxygen can be reactivated by warming up the sample to room temperature again. However, we avoided tuning the doping level this way because such a process is often accompanied by enhanced inhomogeneity, presumably because the BSCCO flakes were covered by h-BN and oxygen could only leak out from the side. The relatively thick BSCCO samples were fabricated from either the optimally doped (S6, S7) or underdoped (S8, S9) single crystals.

Thickness characterization. We employed the atomic force microscope in the contact mode to determine the thicknesses (S1-S5) after the transport measurements. For a

better characterization, we peeled off the h-BN capping layers from the ultrathin samples. Supplementary Figure 2 shows the representative results of S2, S3 and S5. These three samples were determined to be 1.5 UC or 2 UC thick. We note that the apparent height is slightly larger than the expected thickness, presumably due to the different work functions³⁰.

Transport measurements. The magnetotransport and thermoelectric measurements were carried out in two closed-cycle cryogenic systems (base temperature 1.55 K) equipped with superconducting magnets (9 T and 12 T). Electrical resistances were measured in a four-terminal configuration by using the standard lock-in technique (1 μ A at 3.777 or 7.777 Hz).

For thermoelectric measurements, the calibration of the thermometers was carried out in the absence of BSCCO flakes. Specifically, we first measured the temperature dependent resistances of the two thermometers (Th1 and Th2) in the isothermal situation (Supplementary Figure 1a). We then passed an AC current I_{ac} (1 to 8 mA, $\omega/2\pi=3.777$ Hz) through the local heater (Fig. 1b). This heating current gave rise to a temperature gradient oscillating between zero and δT_{1-2} at a frequency of 2ω (with a phase delay of $\pi/2$) across the two thermometers. Experimentally, we measured the variations in resistance of the two thermometers, $\Delta R_{1,2} = \Delta V_{1,2}/I_{1,2}$, where $I_{1,2}$ were the DC current (100 μ A) injected into them and $\Delta V_{1,2}$ were the resulting AC voltages in the two thermometers. The local temperature variation at Th1, 2 with a frequency of 2ω was calculated by using $\Delta T_{1,2} = \frac{\Delta R_{1,2}}{dR_{1,2}(T)/dT}$. Supplementary Figure 2b shows the measured temperature difference: $\delta T_{1-2} = \Delta T_1 - \Delta T_2$ at different heating currents. The reproducibility of the calibration was guaranteed by measuring various sets of thermometers on multiple substrates with exactly the same geometry. We note that conventional on-chip thermometry loses sensitivity at sub-10 K regime due to the saturation of resistance. We have recently overcome this bottleneck and extended our thermometry down to 1 K by utilizing the Kondo effect⁵¹.

For the thermoelectricity measurements of BSCCO, we chose a heating current that optimized the signal-to-noise ratio and made sure the thermometry was in the linear response regime (Supplementary Figure 1). Both the longitudinal and transverse thermal voltages (δV_{xx} and δV_{xy}) were recorded by the lock-in amplifiers. For measuring the Nernst effect, the amplitude of I_{ac} at different temperatures was adjusted to keep the temperature difference between the two longitudinal contacts δT_{xx} to be around 30 mK. Here the two longitudinal contacts have a separation of $l_{xx} = 8 \mu\text{m}$. Seebeck and Nernst signals were obtained via $S = -\delta V_{xx}/\delta T_{xx}$ and $N = \delta V_{xy}/\delta T_{xy}$, where $\delta T_{xy} = \delta T_{xx} \cdot W/l_{xx}$ and W was the width of the sample. We obtained the Nernst signals $N(T)$ by anti-symmetrizing the raw data to remove the possible Seebeck contribution mixed into the signal due to slight misalignment of contacts. This is realized via: $N(B) = [N_{raw}^+(B) - N_{raw}^-(-B)]/2$, where $N_{raw}^+(B)$ and $N_{raw}^-(B)$ are traces taken at positive and negative magnetic fields, respectively.

Thermally activated behavior of vortices. In the thermally activated flux flow regime, the resistivity at a fixed magnetic field B follows: $\rho(B, T) = \rho_0(B) e^{-\frac{U(B)}{k_B T}}$. In the Feigelman-Geshkenbein-Larkin model³⁹ that considers 2D collective vortex creeping, the activation energy $U(B)$ follows a logarithmic dependence on the magnetic field: $U(B) = \frac{\Phi_0^2 d}{64\mu_0\pi^2\lambda^2} \ln(B_0/B)$, where d is the thickness of the sample. We can extract λ by using $\lambda = \frac{\Phi_0}{8\pi} \sqrt{\frac{d}{\mu_0(-dU/d(\ln B))}}$. We further estimate the 2D superfluid phase stiffness following the formula: $\rho_s = \frac{\hbar^2 d}{4\mu_0 k_B e^2 \lambda^2}$. We point out that another model which considers the motion of thermally activated vortex-antivortex pairs⁵² in 2D also gives rise to logarithmic dependence of $U(B)$. There, too, the activation energy is proportional to $1/\lambda^2$ such that the linear doping dependence of ρ_s would not be affected.

Nernst effect due to vortex flow. In deriving the formula for transport entropy per

vortex $S_d = N\Phi_0/\rho_{xx}$, it is often assumed^{18,19,21} that the thermal force on a vortex is balanced by viscosity such that $-S_d\nabla_x T = \eta v_x$, where η is the viscosity coefficient. The Nernst signal is therefore:

$$N = BS_d/\eta. \quad (1)$$

However, the drifting vortex can experience the Magnus force. Consequently, it is the total force—the sum of thermal force and Magnus force—that becomes balanced by the viscous force. H.-C. Ri *et al.*⁵³ considered both the above-mentioned effect and the Hall effect of unbound quasi-particles. They obtained the following equation for the Nernst signal:

$$N = \frac{S_d\rho_{xx}}{\Phi_0} + S_n \frac{\rho_{xx}}{\rho_n} (\tan \theta_{QP} - \tan \theta_V), \quad (2)$$

where S_n is the Seebeck coefficient in the normal state, ρ_n is the normal state resistivity, θ_{QP} and θ_V are the Hall angles for vortices and quasi-particles, respectively. Equation (2) indicates that there exists an additional term that may contribute to the Nernst signal. We note that the two Hall angles are equal in the Bardeen-Stephen model⁵³ such that the second term is zero. Furthermore, the second term has a different temperature dependence than the first one in Eq. (2). If this term has a noticeable contribution, the temperature dependent Nernst effect should exhibit a shoulder instead of a single peak⁵³. Experimentally, we observe no such a shoulder in our data (Fig. 3b1-b5). We therefore neglect the second term in evaluating the vortex entropy.

Theoretical calculation of vortex entropy. Sergeev, Reizer and Mitin derived the following formula for the vortex entropy⁴⁵:

$$S_d = -\pi\xi^2 \frac{\partial}{\partial T} \frac{B_c^2}{2\mu_0}, \quad (3)$$

where μ_0 is the magnetic vacuum permeability. This formula considers the core energy of the vortex and neglects the contribution from the surrounding supercurrent. They argued that the supercurrent does not transport entropy. Following this expression, Rischau *et al.* derived that²²:

$$S_d = -\frac{\Phi_0}{2\mu_0 \ln \kappa} \frac{\partial B_{c1}}{\partial T}. \quad (4)$$

Here B_{c1} is the lower critical magnetic field and $\kappa = \lambda_0/\xi_0$ is the Ginzburg-Landau parameter. In deriving Eq. (4), they used the relations⁵⁴: $B_{c2} = B_c \cdot \sqrt{2} \kappa$, $B_{c1} = B_c \cdot \ln \kappa / (\sqrt{2} \kappa)$, and $B_{c2} = \Phi_0 / (2\pi \xi^2)$. In order to compare the theoretical value with our data at different doping levels, we aim at expressing S_d by physical quantities that can be directly determined by our experiment (apart from physical constants). To do so, we input the relation $B_{c1} = B_{c2} \cdot \ln \kappa / (2\kappa^2)$ back to Eq. (4) and obtain:

$$S_d = -\frac{\Phi_0}{4\mu_0 \kappa^2} \frac{\partial B_{c2}}{\partial T}. \quad (5)$$

By further employing $B_{c2} = B_{c2}(0)(1 - T/T_c)$ and $B_{c2}(0) = \Phi_0 / (2\pi \xi_0^2)$, we derive that:

$$S_d = \frac{\Phi_0^2}{8\pi\mu_0 \lambda_0^2 T_c}. \quad (6)$$

In Eq. (6), both the London penetration depth and the superconducting transition temperature are experimentally measurable quantities.

Data availability

The data generated in this study have been deposited in: <https://doi.org/10.6084/m9.figshare.24581010>. All other data that support the plots within this paper are available from the corresponding author upon request.

Code availability

The computer code used for data analysis is available upon request from the corresponding author.

References

1. Song, C. -L., Wang, Y. -L., Cheng, P., Jiang, Y. -P., Li, W., Zhang, T., Li. Z., He, K., Wang, L., Jia, J.-F., Hung, H.-H., Wu, C., Ma, X. -C., Chen, X. & Xue, Q. -K. Direct observation of nodes and twofold symmetry in FeSe superconductor. *Science* **332**, 1410-1413 (2011).
2. Chen, C., Liu, Q., Bao, W. C., Yan, Y., Wang, Q. H., Zhang, T. & Feng, D. Observation of discrete conventional Caroli–de Gennes–Matricon states in the vortex core of single-layer FeSe/SrTiO₃. *Phys. Rev. Lett.* **124**, 097001 (2020).
3. Sun, H. -H., Zhang, K. -W., Hu, L. -H., Li, C., Wang, G.- Y., Ma, H. -Y., Xu, Z. -A., Gao, C. -L., Guan, D.-D., Li, Y. -Y., Liu, C., Qian, D., Zhou Y., Fu, L., Li, S. -C., Zhang, F.- C. & Jia, J. -F. Majorana zero mode detected with spin selective Andreev reflection in the vortex of a topological superconductor. *Phys. Rev. Lett.* **116**, 257003 (2016).
4. Machida, T., Sun, Y., Pyon, S., Takeda, S., Kohsaka, Y., Hanaguri, T., Sasagawa, T & Tamegai, T. Zero-energy vortex bound state in the superconducting topological surface state of Fe(Se,Te). *Nat. Mater.* **18**, 811–815 (2019).
5. Lee, CS., Jankó, B., Derényi, I. & Barabási, A.-L. Reducing vortex density in superconductors using the ‘ratchet effect’. *Nature* **400**, 337–340 (1999).
6. Wang, Y.-L. Ma, X., Xu, J., Xiao, Z. L., Snezhko, A., Divan, R., Ocola, L. E., Pearson, J. E., Janko, B. & Kwok, W. K. Switchable geometric frustration in an artificial-spin-ice-superconductor heterosystem. *Nat. Nano.* **13**, 560-565 (2018).
7. Lustikova, J., Shiomi, Y., Yokoi, N., Kabeya, N., Kimura, N., Ienaga, K., Kaneko, S., Okuma, S., Takahashi, S. & Saitoh, E. Vortex rectenna powered by environmental fluctuations. *Nat. Commun.* **9**, 4922 (2018).
8. Itahashi, Y. M., Saito, Y., Ideue, T., Nojima, T. & Iwasa, Y. Quantum and classical ratchet motions of vortices in a two-dimensional trigonal superconductor. *Phys. Rev. Res.* **2**, 023127 (2020).
9. Zhang, E., Xu, X., Zou, Y. C., Ai, L., Dong, X., Huang, C., Leng, P., Liu, S., Zhang, Y., Jia, Z., Peng, X., Zhao, M., Yang, Y., Li, Z., Guo, H., Haigh, S. J., Nagaosa, N., Shen, J. & Xiu, F. Nonreciprocal superconducting NbSe₂ antenna. *Nat. Commun.* **11**, 5634

- (2020).
10. Villegas, J. E., Savel'ev, S., Nori, F., Gonzalez, E. M., Anguita, J. V., Garcia, R. & Vicent, J. L. A superconducting reversible rectifier that controls the motion of magnetic flux quanta. *Science* **302**, 1188-1191 (2003).
 11. de Souza Silva, C. C., Van de Vondel, J., Morelle, M. & Moshchalkov, V. V. Controlled multiple reversals of a ratchet effect. *Nature* **440**, 651-654 (2006).
 12. Hoshino, S., Wakatsuki, R., Hamamoto, K. & Nagaosa, N. Nonreciprocal charge transport in two-dimensional noncentrosymmetric superconductors. *Phys. Rev. B* **98**, 054510 (2018).
 13. Xu, J. -P., Wang, M. -X., Liu, Z. L., Ge, J. -F., Yang, X., Liu, C., Xu, Z. A., Guan, D., Gao, C. L., Qian, D., Liu, Y., Wang, Q. -H., Zhang, F. -C., Xue, Q. -K. & Jia, J. -F. Experimental detection of a Majorana mode in the core of a magnetic vortex inside a topological insulator-superconductor $\text{Bi}_2\text{Te}_3/\text{NbSe}_2$ heterostructure. *Phys. Rev. Lett.* **114**, 017001 (2015).
 14. Lv, Y. -F., Wang, W. -L., Zhang, Y. -M., Ding, H., Li, W., Wang, L., He, K., Song, C. -L., Ma, X. -C. & Xue, Q. -K. Experimental signature of topological superconductivity and Majorana zero modes on $\beta\text{-Bi}_2\text{Pd}$ thin films. *Science bulletin*, **62**, 852-856 (2017).
 15. Yuan, Y., Pan, J., Wang, X., Fang, Y., Song, C. -L., Wang, L., He, K., Ma, X. -C., Zhang, H., Huang, F., Li, W. & Xue, Q. -K. Evidence of anisotropic Majorana bound states in 2M-WS_2 . *Nat. Phys.* **15**, 1046–1051 (2019).
 16. Liu, Q., Chen, C., Zhang, T., Peng, R., Yan, Y.- J., Wen, C.-H.-P., Lou, X., Huang, Y. -L., Tian, J. -P., Dong, X. -L., Wang, G. -W., Bao, W. -C., Wang, Q. -H., Yin, Z. -P., Zhao, Z. -X. & Feng, D. -L. Robust and clean Majorana zero mode in the vortex core of high-temperature superconductor $(\text{Li}_{0.84}\text{Fe}_{0.16})\text{OHFeSe}$. *Phys. Rev. X*, **8**, 041056 (2018).
 17. Kong, L., Cao, L., Zhu, S., Papaj, M., Dai, G., Li, G., Fan, P., Liu, W., Yang, F., Wang, X., Du, S., Jin, C., Fu, L., Gao, H. & Ding, H. Majorana zero modes in impurity-assisted vortex of LiFeAs superconductor. *Nat. Commun.* **12**, 4146 (2021).
 18. Wang, Y., Li, L. & Ong, N. P. Nernst effect in high- T_c superconductors. *Phys. Rev. B*

- 73**, 024510 (2006).
19. Behnia, K. & Aubin, H. Nernst effect in metals and superconductors: a review of concepts and experiments. *Rep. Prog. Phys.* **79**, 046502 (2016).
 20. Behnia, K. *Fundamentals of Thermoelectricity* (Oxford Univ. Press, 2015).
 21. Li, X. -Q., Li, Z. -L., Zhao, J. -J. & Wu, X. -S. Electrical and thermoelectric study of two-dimensional crystal of NbSe₂. *Chinese Phys. B* **29**, 087402 (2020).
 22. Rischau, C. W., Li, Y., Fauqué, B., Inoue, H., Kim, M., Bell, C., Hwang, H. Y., Kapitulnik, A. & Behnia, K. Universal bound to the amplitude of the vortex Nernst signal in superconductors. *Phys. Rev. Lett.* **126**, 077001 (2021).
 23. Huebener, R. P. & Ri, H.-C. Vortex transport entropy in cuprate superconductors and Boltzmann constant, *Physica C* **591**, 1353975 (2021).
 24. Jotzu, G., Meier, G., Cantaluppi, A., Cavalleri, A., Pontiroli, D., Riccò, M., Ardavan, A. & Nam, M. -S. Superconducting fluctuations observed far above T_c in the isotropic superconductor K₃C₆₀. *Phys. Rev. X* **13**, 021008 (2023).
 25. Xu, Z. A. Ong, N. P., Wang, Y., Kakeshita, T. & Uchida, S. Vortex-like excitations and the onset of superconducting phase fluctuation in underdoped La_{2-x}Sr_xCuO₄. *Nature* **406**, 486-488 (2000).
 26. Cyr-Choinière, O., Daou, R., Laliberté, F., Collignon, C., Badoux, S., LeBoeuf, D., Chang, J., Ramshaw, B. J., Bonn, D. A., Hardy, W. N., Liang, R., Yan, J.-Q., Cheng, J.-G., Zhou, J.-S., Goodenough, J. B., Pyon, S., Takayama, T., Takagi, H., Doiron-Leyraud, N. & Taillefer, L. Pseudogap temperature T^* of cuprate superconductors from the Nernst effect. *Phys. Rev. B* **97**, 064502 (2018).
 27. Pourret, A., Aubin, H., Lesueur, J., Marrache-Kikuchi, C. A., Berge, L., Dumoulin, L. & Behnia, K. Observation of the Nernst signal generated by fluctuating Cooper pairs. *Nat. Phys.* **2**, 683-686 (2006).
 28. Chang, J., Doiron-Leyraud, N., Cyr-Choinière, O., Grissonnanche, G., Laliberté, F., Hassinger, E., Reid, J-Ph., Daou, R., Pyon, S., Takayama, T., Takagi, H. & Taillefer, L. Decrease of upper critical field with underdoping in cuprate superconductors. *Nat. Phys.* **8**, 751-756 (2012).

29. Tafti, F. F., Laliberté, F., Dion, M., Gaudet, J., Fournier, P. & Taillefer, L. Nernst effect in the electron-doped cuprate superconductor $\text{Pr}_{2-x}\text{Ce}_x\text{CuO}_4$: Superconducting fluctuations, upper critical field H_{c2} , and the origin of the T_c dome. *Phys. Rev. B* **90**, 024519 (2014).
30. Jiang, D., Hu, T., You, L., Li, Q., Li, A., Wang, H., Mu, G., Chen, Z., Zhang, H., Yu, G., Zhu, J., Sun, Q., Lin, C., Xiao, H., Xie, X. & Jiang, M. High- T_c superconductivity in ultrathin $\text{Bi}_2\text{Sr}_2\text{CaCuO}_{8+x}$ down to half-unit-cell thickness by protection with graphene. *Nat. Commun.* **5**, 5708 (2014).
31. Liao, M., Zhu, Y., Zhong, R., Schneeloch, J., Gu, G., Jiang, K., Zhang, D., Ma, X.-C. & Xue, Q.-K. Superconductor–insulator transitions in exfoliated $\text{Bi}_2\text{Sr}_2\text{CaCu}_2\text{O}_{8+\delta}$ flakes. *Nano Lett.* **18**, 5660–5665 (2018).
32. Yu, Y., Ma, L., Cai, P., Zhong, R., Ye, C., Shen, J., Gu, G., Chen, X. H. & Zhang, Y. High-temperature superconductivity in monolayer $\text{Bi}_2\text{Sr}_2\text{CaCu}_2\text{O}_{8+\delta}$. *Nature* **575**, 156–163 (2019).
33. Zhao, S. Y. F., Poccia, N., Panetta, M. G., Yu, C., Johnson, J. W., Yoo, H., Zhong, R., Gu, G., Watanabe, K., Taniguchi, T., Postolova, S. V., Vinokur, V. M. & Kim, P. Sign-reversing Hall effect in atomically thin high-temperature $\text{Bi}_{2.1}\text{Sr}_{1.9}\text{CaCu}_{2.0}\text{O}_{8+\delta}$ superconductors. *Phys. Rev. Lett.* **122**, 247001 (2019).
34. Liao, M., Zhu, Y., Hu, S., Zhong, R., Schneeloch, J., Gu, G., Zhang, D. & Xue, Q.-K. Little-Parks like oscillations in lightly doped cuprate superconductors. *Nat. Commun.* **13**, 1316 (2022).
35. Palstra, T. T. M., Batlogg, B., Schneemeyer, L. F. & Waszczak, J. V. Thermally activated dissipation in $\text{Bi}_{2.2}\text{Sr}_2\text{Ca}_{0.8}\text{Cu}_2\text{O}_{8+\delta}$. *Phys. Rev. Lett.* **61**, 1662 (1988).
36. Briceo, G., Crommie, M. F. & Zettl, A. Giant out-of-plane magnetoresistance in Bi-Sr-Ca-Cu-O: A new dissipation mechanism in copper-oxide superconductors? *Phys. Rev. Lett.* **66**, 2164 (1991).
37. Busch, R., Ries, G., Werthner, H., Kreiselmeyer, G. & Saemann-Ischenko, G. New aspects of the mixed state from six-terminal measurements on $\text{Bi}_2\text{Sr}_2\text{CaCu}_2\text{O}_x$ single crystals. *Phys. Rev. Lett.* **69**, 522 (1992).

38. Clem, J. R. Two-dimensional vortices in a stack of thin superconducting films: A model for high-temperature superconducting multilayers. *Phys. Rev. B* **43**, 7837 (1991).
39. Feigel'man, M.V., Geshkenbein, V.B. & Larkin, A.I. Pinning and creep in layered superconductors. *Physica C* **167**, 177 (1990).
40. Uemura, Y. J., Luke, G. M., Sternlieb, B. J., Brewer, J. H., Carolan, J. F., Hardy, W. N., Kadono, R., Kempton, J. R., Kiefl, R. F., Kretzmann, S. R., Mulhern, P., Riseman, T. M., Williams, D. Li., Yang, B. X., Uchida, S., Takagi, H., Gopalakrishnan, J., Sleight, A. W., Subramanian, M. A., Chien, C. L., Cieplak, M. Z., Xiao, G., Lee, V. Y., Statt, B. W., Stronach, C. E., Kossler, W. J. & Yu, X. H. Universal correlations between T_c and n_s/m^* (carrier density over effective mass) in high- T_c cuprate superconductors. *Phys. Rev. Lett.* **62**, 2317 (1989).
41. Jacobs, T., Sridhar, S., Li, Q., Gu, G. D. & Koshizuka, N. In-plane and c -axis microwave penetration depth in $\text{Bi}_2\text{Sr}_2\text{Ca}_1\text{Cu}_2\text{O}_{8+\delta}$ crystals. *Phys. Rev. Lett.* **75**, 4516 (1995).
42. Kogan, V. G., Ledvij, M., Simonov, A. Yu., Cho, J. H. & Johnston, D. C. Role of vortex fluctuations in determining superconducting parameters from magnetization data for layered superconductors. *Phys. Rev. Lett.* **70**, 1870 (1993).
43. Lee, S. L., Zimmermann, P., Keller, H., Warden, M., Savic, I. M., Schauwecker, R., Zech, D., Cubitt, R., Forgan, E. M., Kes, P. H., Li, T. W., Menovsky, A. A. & Tarnawski, Z. Evidence for flux-lattice melting and a dimensional crossover in single-crystal $\text{Bi}_{2.15}\text{Sr}_{1.85}\text{CaCu}_2\text{O}_{8+\delta}$ from muon spin rotation studies. *Phys. Rev. Lett.* **71**, 3862 (1993).
44. Behnia, K. Nernst response, viscosity and mobile entropy in vortex liquids. *J. Phys.: Condens. Matter* **35** 074003 (2023).
45. Sergeev, A., Reizer, M. & Mitin, V. Thermomagnetic vortex transport: Transport entropy revisited. *Europhys. Lett.* **92**, 27003 (2010).
46. Hoffman, J. E., Hudson, E. W., Lang, K. M., Madhavan, V., Eisaki, H., Uchida, S. & Davis, J. C. A Four Unit Cell Periodic Pattern of Quasi-Particle States Surrounding Vortex Cores in $\text{Bi}_2\text{Sr}_2\text{CaCu}_2\text{O}_{8+\delta}$. *Science* **295**, 466-469 (2002).

47. Machida, T., Kohsaka, Y., Matsuoka, K., Iwaya, K., Hanaguri, T. & Tamegai, T. Bipartite electronic superstructures in the vortex core of $\text{Bi}_2\text{Sr}_2\text{CaCu}_2\text{O}_{8+\delta}$. *Nat Commun* **7**, 11747 (2016).
48. Edkins, S. D., Kostin, A., Fujita, K., Mackenzie, A. P., Eisaki, H., Uchida, S., Sachdev, S., Lawler, M. J., Kim, E. -A., Davis, J. C. S. & Hamidian, M. H. Magnetic field–induced pair density wave state in the cuprate vortex halo. *Science* **364**, 976-980 (2019).
49. Ussishkin, I., Sondhi, S. L. & Huse, D. A. Gaussian superconducting fluctuations, thermal transport, and the Nernst effect. *Phys. Rev. Lett.* **89**, 287001 (2002).
50. Glatz, A. Pourret, A. & Varlamov, A. A. Analysis of the ghost and mirror fields in the Nernst signal induced by superconducting fluctuations. *Phys. Rev. B* **102**, 174507 (2020).
51. Qiao, J. & Zhang, D. Extension of on-chip thermometry of metal strips toward sub-10 K regime. *Appl. Phys. Lett.* **120**, 173507 (2022).
52. Jensen, H.J., Minnhagen, P., Sonin, E. & Weber, H. Vortex fluctuations, negative Hall effect, and thermally activated resistivity in layered and thin-film superconductors in an external magnetic field. *Europhys. Lett.* **20**, 463 (1992).
53. Ri. H. -C., Kober, F., Beck, A., Alff, L. Gross, R. & Huebener, R. P. Thermal diffusion of quasiparticles and vortices in the mixed state of high-temperature superconductors. *Phys. Rev. B* **47**, 12312 (1993).
54. Tinkham, M. *Introduction to superconductivity* (Courier Corporation, 1996).
55. Logvenov, G. Y., Kartsovnik, M. V., Ito, H., & Ishiguro, T. Seebeck and Nernst effects in the mixed state of the two-band organic superconductors κ -(BEDT-TTF) $_2$ Cu(NCS) $_2$ and κ -(BEDT-TTF) $_2$ Cu[N(CN) $_2$]Br. *Met. Synth.* **86**, 2023 (1997).
56. Pourret, A., Malone, L., Antunes, A. B., Yadav, C. S., Paulose, P. L., Fauqu e, B. & Behnia, K. Strong correlation and low carrier density in $\text{Fe}_{1+\gamma}\text{Te}_{0.6}\text{Se}_{0.4}$ as seen from its thermoelectric response. *Phys. Rev. B* **83**, 020504(R) (2011).
57. Capan, C., Behnia, K., Hinderer, J., Jansen, A. G. M., Lang, W., Marcenat, C., Marin, C. & Flouquet, J. Entropy of vortex cores near the superconductor-insulator transition in an underdoped cuprate. *Phys. Rev. Lett.* **88**, 056601 (2002).

58. Gollnik, F., & Naito, M. Doping dependence of normal-and superconducting-state transport properties of $\text{Nd}_{2-x}\text{Ce}_x\text{CuO}_{4\pm y}$ thin films. *Phys. Rev. B* **58**, 11734 (1998).
59. de Lange, O. L. & Otter, F. A. Flux flow effects in a nearly reversible type II superconductor. *J. Low Temp. Phys.* **18**, 31-42 (1975).

Acknowledgements

We thank fruitful discussions with Haiwen Liu and Zhu'an Xu. This work is financially supported by the Ministry of Science and Technology of China (2022YFA1403103) and the National Natural Science Foundation of China (Grants Nos. 12361141820, 12274249, 12204045, 52388201, and 52011530393) and. J.Q. was supported by Beijing Institute of Technology Research Fund Program for Young Scholars. Work at Brookhaven is supported by the Office of Basic Energy Sciences, Division of Materials Sciences and Engineering, U. S. Department of Energy under Contract No. DE-SC0012704.

Author contributions

S.H. and J.Q. initiated the project, fabricated the samples and carried out transport measurements. G.G. grew the single crystals. S.H, J.Q. and D.Z. analyzed the data and wrote the paper with input from Q.-K.X.

Competing interests

The authors declare no competing interests.

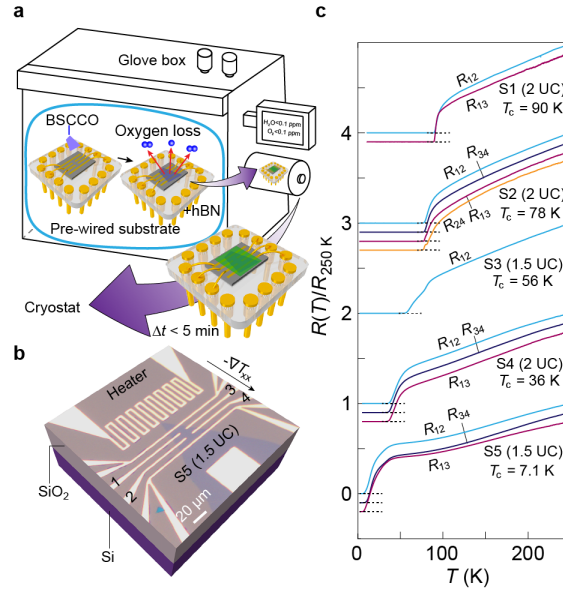


Figure 1 Fabrication and characterization of ultrathin BSCCO. **a**, Key fabrication steps in a glovebox with inert atmosphere for realizing ultrathin BSCCO flakes with different doping levels. Purple arrows indicate the work-flow. The BSCCO flake is dry-transferred onto a substrate with prepatterned electrodes that are already wired to the chip carrier. Red arrows schematically illustrate the out-diffusion of interstitial oxygen in BSCCO. In the end of the process, the complete chip is taken out of the glovebox and plugged in the measurement stick and loaded into the cryostat within 5 minutes. **b**, Optical image of sample S5 together with electrodes for resistance and thermoelectric measurements. Numbers mark the electrodes for measuring the resistance. Arrow indicates the direction of the temperature gradient if the heater is on. **c**, Normalized resistance as a function of temperature for five ultrathin samples (S1-S5). Thicknesses are indicated in the parentheses. For some samples, resistance data from different pairs of electrodes are included. The subscripts indicate the used contacts. For example, R_{12} represents the resistance between electrodes 1 and 2 (indicated in panel b). R_{13} and R_{24} are mainly from the longitudinal component that mixes into the transverse resistance due to slight misalignment between the current and the Hall contacts. Curves are vertically offset for clarity. Dashed lines mark zero resistance for each curve. For each sample, T_C is defined as the temperature point where the resistance reaches 1% of the normal state resistance.

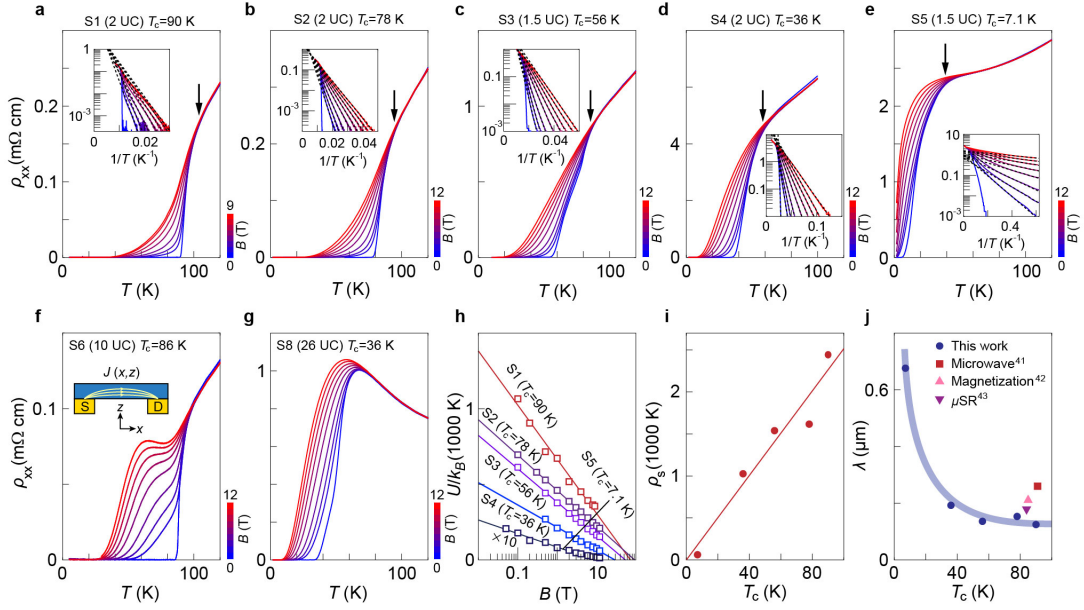


Figure 2 Resistivity signals in ultrathin BSCCO with different doping levels. Temperature dependent resistivity of ultrathin samples S1-S5 (**a-e**) and bulk-like samples S6 and S8 (**f,g**) at a set of perpendicular magnetic fields (B). (For S1, $B = 0, 0.5, 1, 2, 4, 6, 8, 9$ T; For S2-S6 and S8, $B = 0, 0.5, 1, 2, 4, 6, 8, 10, 12$ T.) Insets of **a-e** show Arrhenius plots of the data. Arrows in **a-e** mark the temperature point where the resistivity traces bifurcate. Dashed lines are linear fits. Inset in **f** shows the schematic drawing of the current distribution in thick BSCCO flakes. **h**, Activation energy U/k_B as a function of B for samples S1-S5. Solid lines are linear fits. **i**, Superfluid phase stiffness ρ_s as a function of T_c . Solid line is a linear fit that crosses the origin. **j**, London penetration depth λ as a function of T_c . Circles are depth values evaluated from the phase stiffness. Other symbols are depth values from former studies⁴¹⁻⁴³ on BSCCO single crystals. These parameters are given in Supplementary Table S1.

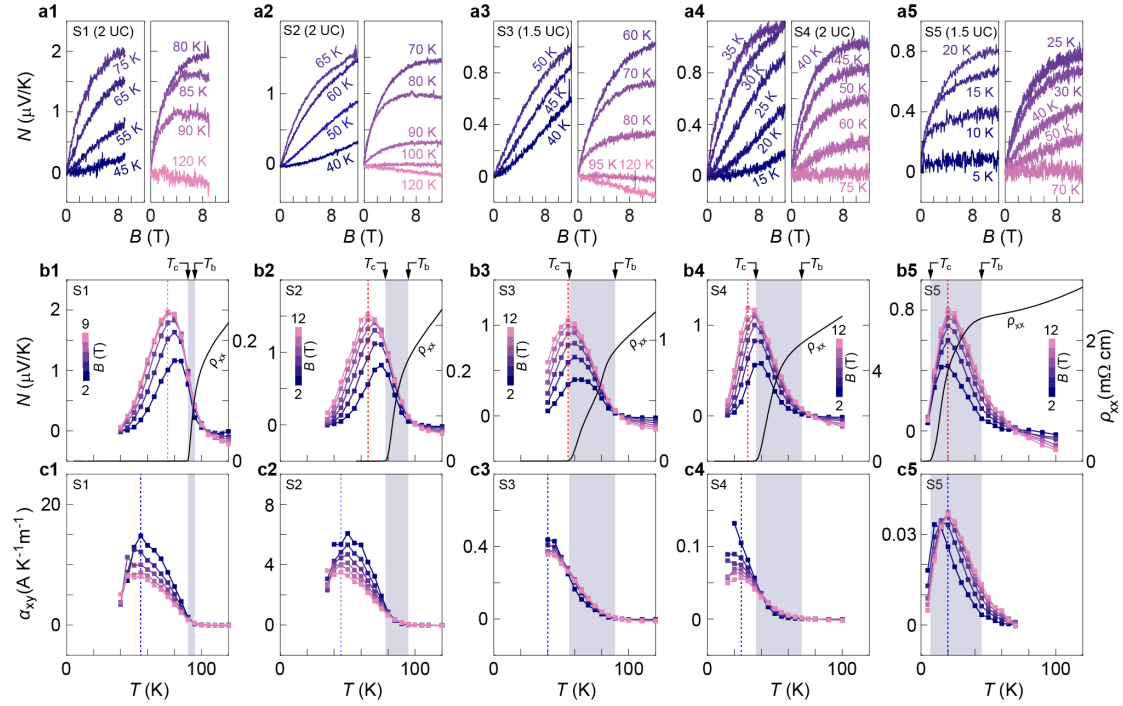


Figure 3 Nernst signals and off-diagonal Peltier coefficients in ultrathin BSCCO with different doping levels. **a1-a5**, Nernst signals as a function of B at selected temperature points for samples S1 to S5. **b1-b5**, Nernst signals as a function of temperature at fixed B (For S1, $B = 2, 4, 6, 8, 9$ T; For S2-S5, $B = 2, 4, 6, 8, 10, 12$ T). Red dotted lines mark peak positions of N at the maximum B . Dashed lines mark T_c defined from resistivity data. Black traces are zero-field resistivity data. Values of N at each B are obtained by averaging the data points on the $N(B)$ trace. For $B < 9$ T in S1 and $B < 12$ T in S2-S5, we take the average in the window of $[B - 0.5, B + 0.5]$ T. For the maximum B , a window of $[B - 0.5, B]$ T is chosen. **c1-c5**, Off-diagonal Peltier coefficients α_{xy} as a function of temperature at fixed B (same color coding as panels **b1-b5**). Blue dotted lines mark peak positions of α_{xy} at the maximum B . Dashed lines mark T_c . Shaded regions in **b1-b5** and **c1-c5** represent the temperature window from T_c to T_b . The latter temperature is defined as the point above which N from superconducting fluctuations drops below the measurement noise level (Supplementary Note 6).

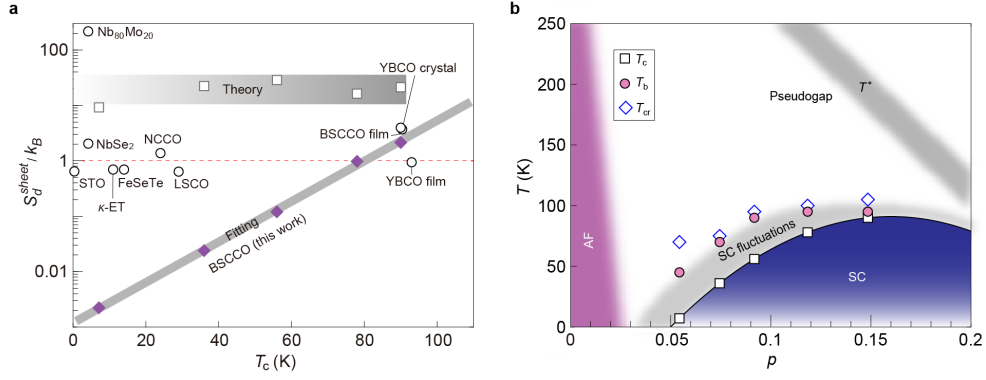


Figure 4 Sheet entropy of vortices and superconducting fluctuations. a, Sheet entropy as a function of T_c for a variety of superconductors. Diamonds are data from 2D BSCCO of this work. These values are evaluated at peak positions of N for S1 to S4 and at 5 K for S5 at the maximum magnetic field (9 T for S1, 12 T for S2-S5). Gray solid line is an exponential fit to the data. Squares indicate the theoretically evaluated entropy. Circles are entropy values at the Nernst peak positions from former studies: STO ($\text{SrTi}_{0.99}\text{Nb}_{0.01}\text{O}_3$)²², κ -ET (κ -(ET)₂Cu[N(CN)₂]Br)⁵⁵, FeSeTe ($\text{FeSe}_{0.6}\text{Te}_{0.4}$)⁵⁶, LSCO ($\text{La}_{1.92}\text{Sr}_{0.08}\text{CuO}_4$)⁵⁷, NCCO ($\text{Nd}_{1.85}\text{Ce}_{0.15}\text{CuO}_{4+\gamma}$)⁵⁸, YBCO single crystal and epitaxially grown film²³, epitaxially grown BSCCO film²³, NbSe_2 ²¹, $\text{Nb}_{80}\text{Mo}_{20}$ ⁵⁹. We note that the first five materials were addressed in ref²² and ref⁴⁴. Parameters used here are provided in Supplementary Table S2. **b**, Summary of the superconducting fluctuation regime in the typical superconducting phase diagram of cuprates. Squares/circles/diamonds represent $T_{c,b,cr}$, respectively. The doping level p is evaluated from the empirical relation $T_c = 91 \cdot [1 - 82.6(p - 0.16)^2]$.